

# Revealing Point Group Symmetry of Rare-earth Dopants via Polarization-resolved Single-particle Microspectroscopy

Peng Li<sup>1,2,†\*</sup>, Yaxin Guo<sup>2,†</sup>, Yaoxu Yan<sup>3</sup>, Fu Liu<sup>2,\*</sup>, Yanpeng Zhang<sup>2</sup>, Feng Yun<sup>2,4</sup>, Rongqian Wu<sup>1</sup>, Yi Lyu<sup>1</sup>, Feng Li<sup>2,4\*</sup>

<sup>1</sup>Institute of Regenerative and Reconstructive Medicine, Med-X Institute, The First Affiliated Hospital of Xi'an Jiaotong University, Xi'an 710061, China

<sup>2</sup>Key Laboratory for Physical Electronics and Devices of the Ministry of Education and Shaanxi Key Lab of Information Photonic Technique, School of Electronic Science and Engineering, Faculty of Electronic and Information Engineering, Xi'an Jiaotong University, Xi'an 710049, China

<sup>3</sup>State Key Laboratory of Modern Optical Instrumentation, CNERC for Optical Instruments, Zhejiang University, 38 Zheda Road, Xihu District, Hangzhou 310027, China

<sup>4</sup>Solid-State Lighting Engineering Research Center, Xi'an Jiaotong University, Xi'an 710049, China

†These authors contributed equally: Peng Li, Yaxin Guo

\*Correspondence to: [ponylee@xjtu.edu.cn](mailto:ponylee@xjtu.edu.cn), [fu.liu@xjtu.edu.cn](mailto:fu.liu@xjtu.edu.cn), [felix831204@xjtu.edu.cn](mailto:felix831204@xjtu.edu.cn)

**Abstract:** The local point group symmetry of luminescent centers, such as defects, impurities, and dopant ions within a crystal, dictates their optical transition properties. While conventional low-temperature spectroscopy quantifies point group symmetry by enumerating the splitting of optical transitions, it fails to capture vectorial symmetry information, such as the orientation of symmetry axes. Here, we establish a quantitative link between point group symmetry, crystal symmetry, optical transition dipole orientation, and polarized luminescence in rare-earth-doped single-particle crystals using computational electromagnetism. Combined with room-temperature single-particle polarization spectroscopy, we resolve the magnetic dipole orientations from individual optical transition of dopant ions in single microcrystal, enabling precise identification of point group symmetry and its axes. We observe single-particle chirality arising from spontaneous symmetry breaking of intrinsically chiral space group during crystallization. Based on point group and crystal symmetries, we present a practical scheme to optical sensing the 3D orientation of rare-earth-doped single particles in dynamic environments by using two arbitrarily transition bands from single-view polarization spectra. Our computational electromagnetism framework not only elucidates polarized luminescence but also provides insights into optimizing dipole orientation-dependent energy transfer for designing ultra-bright rare-earth-doped nanocrystals, such as Förster resonance energy transfer, and can interpret enhanced linear polarization in extreme optical phenomena like stimulated emission, superradiance, and superfluorescence following dipole-coherent radiation in single emitters.

## Introduction

Symmetry principle has profoundly influenced human civilization, permeating and becoming deeply ingrained within core domains of human activity, including architecture, music, literature, art, and the natural sciences<sup>1</sup>. In the physical world, symmetry is crucial in determining the fundamental forces, a principle often referred to as symmetry-dictated interaction<sup>2</sup>. Numerous fundamental laws and theories in physics are derived from analyzing the symmetries of systems. Notable examples include special and general relativity founded on spacetime symmetries<sup>3,4</sup>, quantum numbers and selection rules arising from the symmetries of quantum systems<sup>5</sup>, and the Standard Model constructed upon a gauge theory of symmetry breaking<sup>6</sup>. Crystallography constitutes a key area of research in physics, with the rich and complex symmetries of crystals described by space groups and point groups<sup>7</sup>. Crystals belonging to the same space group exhibit a wide range of common mechanical, thermal, and

electrical properties. For luminescent centers within a crystal, such as defects, impurities, and dopant ions, the local point group symmetry (the symmetry of the surrounding crystalline environment) governs their electronic structure<sup>8-10</sup>. This, in turn, determines the wavelength, relative intensities, spectral splitting, and polarization properties of optical transitions<sup>11-13</sup>. As elegantly articulated by physicist Eugene Wigner, “It is one of the most remarkable discoveries of the last hundred years that the inherent laws of spectroscopy are dictated by the symmetry properties of the system in question.”<sup>14</sup>

The unique optical properties arising from point group symmetries underpin the widespread application of rare-earth-doped crystals in advanced optical technologies, including displays<sup>15-18</sup>, lasers<sup>19-21</sup>, super-resolution imaging<sup>22-28</sup>, ultrasmall force measurements<sup>29-31</sup>, microscopic rotation sensing<sup>32-34</sup>, and quantum photonics<sup>35-41</sup>. Traditionally, crystallographers have employed single-crystal X-ray diffraction data to construct models of the microscopic structure of crystals, thereby determining the point group symmetry at a given lattice site<sup>42</sup>. However, over the past decade, the breaking of point group symmetry has been widely observed in rare-earth-doped crystals<sup>43</sup>. This symmetry breaking, occurring at the atomic scale, exhibits a concealed, localized character ( $< 1 \text{ nm}^3$ ), rendering it undetectable by average crystallographic techniques such as single-crystal or powder X-ray diffraction, diffuse X-ray scattering, or neutron diffraction. Given the sensitivity of rare-earth ion optical transitions to the point group symmetry, even subtle symmetry breaking can manifest as an increase in the splitting number of the transitions<sup>11,12,43</sup>. Consequently, researchers have employed cryogenic high-resolution spectroscopy to quantify the point group symmetry by enumerating the spectral splittings of transitions<sup>44</sup>. However, this method provides no information on vectorial symmetry, including the orientation of the symmetry axes. Recently, a theoretical study proposes a “Continuous Symmetry Operations Measurement” (CSOM) algorithm for evaluating point group symmetry<sup>45</sup>. This algorithm requires precise atomic coordinates to assess the actual symmetry by calculating deviations from the ideal symmetry, while also automatically identifying the symmetry axes. However, in crystals exhibiting point group symmetry breaking, as noted above, the local atomic coordinates remain inaccessible via conventional crystallographic techniques. Consequently, this algorithm cannot yet be applied to resolve the actual symmetry characteristics in such systems. Thus, neither cryogenic spectroscopy based on the transition splitting numbers nor theoretical algorithms requiring precise atomic coordinates can fully elucidate the point group symmetry of ions in real crystals, particularly the orientation of the symmetry axes.

In spectroscopy, the point group symmetry breaking not only increases the splitting number but also induces different types of transition dipole for splitting peaks, resulting in different polarizations<sup>11,46,47</sup>. Indeed, as early as the 1960s, researchers observed polarized luminescence in rare-earth-doped bulk crystals, which serves as a valuable tool for both the classification of electromagnetic transition dipole and the quantization of point group symmetry<sup>48-55</sup>. In the early 21st century, the rapid advancement of nanotechnology significantly accelerated the application of rare-earth-doped nanomaterials in nano-optics<sup>15</sup>. However, due to the vectorial nature of polarized luminescence, conventional ensemble spectroscopic techniques are incapable of resolving or detecting the polarization. Over the past decade, single-particle spectroscopy has enabled researchers to observe the polarized emission from rare-earth doped single micro- and nanocrystals<sup>33,47,56-66</sup>, suggesting potential applications such as measurements of microfluidic shear rate and rotational dynamics of biology systems<sup>32-34</sup>. However, these studies rarely explore the fundamental relationship between polarized luminescence, transition dipole orientation, and point group symmetry. The primary challenges lie in establishing a physical model for dipole transitions in single-particle crystals incorporating both the crystal and point group symmetries, as well as analyzing the far-field polarization of single particles through rigorous computational electromagnetism. In one notable study, R. Chacon et al. resolved optical transition dipole orientations in single nanocrystals using high-numerical-aperture Fourier polarization imaging, but did not link them to point group symmetry<sup>62</sup>. Our plane-wave approximation approach confirmed the impact of lattice geometry on dipole orientations but not explicitly connecting them to point group symmetry<sup>47</sup>.

In this study, we present the comprehensive theoretical analysis of far-field polarized emission from rare-earth-doped single-particle crystal in real space, based on rigorous computational electromagnetics. We derive analytical expressions for the far-field polarized intensities, enabling quantitative determination of transition dipole orientations of rare-earth dopants. Combined with high-precision polarization-resolved spectroscopy of single particles at room-temperature, we resolve the magnetic dipole orientations from an optical transition splitting, revealing the point group symmetry of  $\text{Eu}^{3+}$  ions doped within individual  $\text{YPO}_4$  microcrystals. The magnetic dipole orientations directly reveal the axes of point group symmetry, as dictated by optical selection rules, naturally providing information on vectorial symmetry. Moreover, we demonstrate that single-particle optical chirality originates from spontaneous symmetry-breaking of chiral space group during crystallization.

Furthermore, we propose a polarization sensing scheme based on “oriented-dipoles-emitting single-particle antennas”. This approach enables three-dimensional (3D) orientation determination of single particles using only two optical transition bands of rare-earth dopants from single-view polarization spectra. It facilitates real-time monitoring of the 3D orientation dynamics of target objects in microdynamic environments, such as the rotational motion of motor proteins within cells, organelle assembly, DNA conformational transitions, and dynamic remodeling of cytoskeletal structures, including microfilaments and microtubules. Notably, our analysis of transition dipole orientations enables quantitative evaluation of the dipole orientation factor  $\kappa^2$  in Förster energy transfer (FRET)<sup>67,68</sup>. This insight facilitates optimization of energy transfer efficiency through donor-acceptor dipole orientations, paving the way for the design of ultra-bright rare-earth upconversion nanocrystals and other single-particle emitters. Our rigorous computational electromagnetic approach to quantitatively analyze polarized luminescence also enables prediction and interpretation of extreme emission with significantly linear polarization, including superfluorescence<sup>69</sup>, superradiance, and stimulated emission amplification resulting from inherent dipoles coherent transition.

## Results and Discussion

**Theoretical analysis of single-particle polarized luminescence.** The polarized emission of rare-earth-doped single-particle crystals is fundamentally determined by the orientation of inherent optical transition dipoles<sup>33,47,62</sup>. To extract the dipole orientation from polarization spectra, we developed a physical model for single-particle far-field polarized emission. The synthesized  $\text{YPO}_4:\text{Eu}^{3+}$  single microcrystals crystallize in the hexagonal phase (space group  $P6_222$ )<sup>70-74</sup>, with dimensions of approximately 2.5  $\mu\text{m}$  in length and 1.5  $\mu\text{m}$  in diameter (**Supplementary Section I Fig. 1**). The unit cell structure, shown in **Fig. 1a**, contains three layers of  $\text{Y}^{3+}$  ions arranged alternately in an ABCA stacking sequence along the crystalline  $c$ -axis, which coincides with the long axis of the microcrystals. Based on the distribution within the unit cell, we extracted the  $\text{Y}^{3+}$  ions in **Fig. 1b**. Their projection forms a Kagome lattice in the  $x$ - $o$ - $y$  plane (**Fig. 1c**), exhibiting six-fold rotational symmetry. When the  $\text{Y}^{3+}$  ions within a single crystal are partially or fully substituted by  $\text{Eu}^{3+}$  dopants, the  $\text{Eu}^{3+}$  projection maintains the rotational symmetry. Upon excitation,  $\text{Eu}^{3+}$  ions produce a series of optical electric and magnetic dipole transitions. Taking the magnetic dipole transition as an example (consistent with our experiments), we assume a magnetic dipole of an individual  $\text{Eu}^{3+}$  ion forms an angle  $\alpha$  with the crystal

c-axis. Due to the crystal uniformity and rotational symmetry, the magnetic dipoles for all  $\text{Eu}^{3+}$  ions are expected to maintain the same polar angle  $\alpha$  relative to the c-axis. Consequently, under the far-field approximation, the numerous identical magnetic dipoles within the single microcrystal can be effectively represented by dipoles with sixfold rotational symmetry, as shown in **Fig. 1d**.

Under non-resonant excitation (conventional pumping conditions), the transition magnetic dipoles emit incoherently through spontaneous emission, i.e., the dipoles do not oscillate together with a coherent phase. Using rigorous computational electromagnetics, we first analyzed the far-field emission of a single magnetic dipole (**Supplementary Section II Fig. 2**). Then, we derived analytical expressions for the total far-field polarized intensity from such six incoherent magnetic dipoles (**Supplementary Section II Fig. 3**).

$$|E_x|^2 = \frac{3}{r^2} (2\cos^2\alpha \sin^2\theta \sin^2\varphi + \sin^2\alpha \cos^2\theta) \quad (1)$$

$$|E_y|^2 = \frac{3}{r^2} (2\cos^2\alpha \sin^2\theta \cos^2\varphi + \sin^2\alpha \cos^2\theta) \quad (2)$$

$$|E_z|^2 = \frac{3}{r^2} \sin^2\alpha \sin^2\theta \quad (3)$$

Here,  $|E_x|^2$ ,  $|E_y|^2$  and  $|E_z|^2$  represent the polarized intensities along the x, y, and z directions at the detection point  $\vec{r}$ , respectively, where  $(\theta, \varphi)$  are the spherical coordinates of  $\vec{r}$ , as illustrated in the inset of **Fig. 1**. Based on the far-field analytical expressions, we plotted the polarized intensity distributions for both individual magnetic dipoles and their total incoherent emission in **Fig. 2**, and systematically investigated how the polarization evolves with the dipole orientation angle  $\alpha$ . When  $\alpha = 0^\circ$ , as shown in **Fig. 2a**, both the individual dipoles and total incoherent emission are purely linearly polarized perpendicular to the z-axis (crystal c-axis). The total incoherent intensity at each spatial detection point is  $|E_T|^2 = |E_x|^2 + |E_y|^2$ , indicated by the blue region in the upper-right inset. In this case, linear polarization detection along any radial direction of the single crystal, for example, along the x-direction ( $\theta = \pi/2, \varphi = 0$ ), yields a purely linearly polarized intensity  $|E_T|^2 = |E_y|^2$ , as illustrated in the lower-right inset. When  $\alpha$  increases to  $50^\circ$ , as illustrated in **Fig. 2b**, we observe the emergence and enhancement of  $|E_z|^2$  (yellow region), representing purely linearly polarized light with its electric vector parallel to the crystal c-axis. Due to the rotational symmetry of the dipoles around the c-axis, both incoherent  $|E_z|^2$  and  $|E_T|^2$  exhibit rotational symmetry. The coexistence of  $|E_z|^2$  and  $|E_T|^2$  results in partially linearly polarized emission along the radial directions of the

single crystal. Notably, at  $\alpha = 54.7^\circ$ , as shown in **Fig. 2c**, the incoherent  $|E_z|^2$  and  $|E_T|^2$  become equal along the radial directions, leading to completely unpolarized emission of the single crystal. As the  $\alpha$  increases to  $60^\circ$ , as shown in **Fig. 2d**, the linearly polarized intensity  $|E_z|^2$  dominates by surpassing  $|E_T|^2$  along the radial directions. Finally, at  $\alpha = 90^\circ$  (**Fig. 2e**), the incoherent emission along the radial directions consists solely of the pure linearly polarized component  $|E_z|^2$ . From the images in **Fig. 2**, it is apparent that as the magnetic dipole orientation angle increases, the emission along the radial direction of the single crystal evolves from purely linearly polarized (perpendicular to the c-axis), through partially polarized and unpolarized states, to purely linearly polarized (parallel to the c-axis). This transition enables determination of the dipole orientation angle  $\alpha$  from polarization measurements (see analytical expressions below).

In addition to polarization evolution along the radial direction (e.g., the x-direction), we also investigated the polarization of the single crystal detected along the axial direction (z-direction,  $\theta = 0$ ) in detail (**Supplementary Section II Fig. 4**). The analysis reveals that the axial emission is unpolarized, as confirmed by experimental observations<sup>47,59,60,66</sup>. Furthermore, any linear polarization component (e.g.,  $|E_x|^2$  or  $|E_y|^2$ ) emitted along the axial direction equals the radial component  $|E_z|^2$  — a key feature of magnetic dipole transitions in single hexagonal crystals<sup>32,47</sup>. Based on these analyses, **Fig. 2f** plots the normalized intensities of  $|E_y|^2$  and  $|E_z|^2$  emitted along the x-axis (radial direction) and  $|E_x|^2$  emitted along the z-axis (axial direction), as functions of the magnetic dipole orientation angle  $\alpha$ . From the **Eqs. 1–3**,  $|E_y|^2$  and  $|E_z|^2$  emitted along the x-axis ( $\theta = \pi/2$ ,  $\varphi = 0$ ) follow  $\cos^2\alpha$  and  $\sin^2\alpha/2$ , respectively, while  $|E_x|^2$  emitted along the z-axis ( $\theta = 0$ ) follows  $\sin^2\alpha/2$ . Thus, for a single particle measured along its radial direction, the ratio between linearly polarized intensities parallel and perpendicular to the crystal c-axis is

$$\frac{I_{\parallel}}{I_{\perp}} = \frac{|E_z|^2}{|E_y|^2} = \frac{\tan^2\alpha}{2} \quad (4)$$

This expression enables determination of the magnetic dipole orientation from the  $I_{\parallel}$  and  $I_{\perp}$  polarized spectra. However, direct measurement of  $I_{\parallel}$  and  $I_{\perp}$  is challenging for randomly in-plane orientated single micro- and nanocrystals. In this study, we used two continuous polarization detection methods of Polarization Poincaré sphere (PS) and polarization fitting (PF) to obtain the degree of linear polarization (LDOP), which then substitutes for the specific  $I_{\parallel}$  and  $I_{\perp}$ , enabling precise and reliable

dipole orientation determination.

**Two polarized detection methods.** To quantify polarization emission, we established a high-precision polarization-resolved microspectroscopy system (**Supplementary Section III Fig. 6**). Using a low numerical aperture microscope objective (NA = 0.55), we collected photoluminescence from the radial direction of in-plane single microcrystals, and analyzed their polarization in two forms, using the PS and PF methods (**see Methods Section**). The PS method requires measuring three normalized Stokes parameters ( $S_1, S_2, S_3$ ) to determine the polarization state. Here,  $S_1$  and  $S_2$  are used to calculate the linear polarization angle  $\Omega = (\arctan(S_2/S_1))/2$  and degree LDOP =  $\sqrt{S_1^2 + S_2^2}$ , while  $S_3$  is used to assess the optical activity or chirality of the crystal. Using the PS method, we first verified our system accuracy (**Supplementary Section III Fig. 7**). The results of the unpolarized white light characterization confirm the high precision of our system, eliminating the need for polarization error correction.

For the PF method, if the luminescence exhibits no circular polarization component ( $S_3 = 0$ ), it must satisfy the partial linear polarization equation:

$$I_\omega = (A - B)\cos^2(\omega - \Omega) + B \quad (5)$$

or

$$I_\omega = A\cos^2(\omega - \Omega) + B\sin^2(\omega - \Omega) \quad (6)$$

Here,  $A - B$  and  $B$  are positive values representing the purely linearly polarized and unpolarized components, respectively, where  $\omega$  and  $\Omega$  are the detection angle and luminescence angle of linear polarization, respectively. By fitting the measured  $I(\omega)$  data with **Eqs. 5 or 6**, we can obtain the parameters  $A$ ,  $B$ , and  $\Omega$ , which allows us to calculate the linear polarization degree as LDOP =  $(I_{max} - I_{min})/(I_{max} + I_{min}) = (A - B)/(A + B)$ . Using computational electromagnetics, we have theoretically derived the expression for the polarization-resolved radial intensity of the single particle as (**Supplementary Section II Fig. 5**).

$$I_\omega = I_{\parallel}\cos^2(\omega - \Omega_c) + I_{\perp}\sin^2(\omega - \Omega_c) \quad (7)$$

Here,  $\omega$  and  $\Omega_c$  represent the linear polarization detection angle and the crystal c-axis in-plane orientation angle, respectively. Comparison of **Eqs. 6 and 7** reveals that single-particle radial emission is partially linearly polarized, and the fitted  $\Omega$  must equal to  $\Omega_c$  or  $\Omega_c \pm \pi/2$ . If  $\Omega = \Omega_c$ , indicating that the luminescence linear polarization angle aligns with the crystal c-axis, the parameters  $A = I_{\parallel}$



and  $B = I_{\perp}$  yield  $LDOP = (I_{\parallel} - I_{\perp})/(I_{\parallel} + I_{\perp})$ . Substituting this into **Eq. 4** yields:

$$\frac{1+LDOP}{1-LDOP} = \frac{\tan^2 \alpha}{2} \quad (8)$$

Conversely, if  $\Omega = \Omega_c \pm \pi/2$ , where the polarization angle is perpendicular to the crystal c-axis, parameters  $A = I_{\perp}$  and  $B = I_{\parallel}$  result in  $LDOP = (I_{\perp} - I_{\parallel})/(I_{\perp} + I_{\parallel})$ , and substitution into **Eq. 4** provides:

$$\frac{1-LDOP}{1+LDOP} = \frac{\tan^2 \alpha}{2} \quad (9)$$

By comparing the luminescence linear polarization angle  $\Omega$  with the crystal c-axis in-plane orientation angle  $\Omega_c$ , we can resolve the transition magnetic dipole orientation  $\alpha$  through LDOP. Both the PS and PF methods yield the linear polarization angle  $\Omega$  and degree LDOP. Critically, the PS method eliminates crystal optical activity or chirality, while the PF method, based on more extensive  $I(\omega)$  data, provides more stable and precise polarization conclusions.

**Polarized luminescence measurements.** The inset of **Fig. 3a** shows a photoluminescence CCD image of a single hexagonal  $YPO_4:Eu^{3+}$  microcrystal (sample no. 1) with one of the six side facets lying on the substrate, while the crystalline c-axis (long axis) is parallel to the substrate and exhibits the in-plane orientation angle  $\Omega_c$  with approximately  $156^\circ$  (dashed yellow arrow). We defined  $0^\circ$  as the spectrometer slit direction (solid white double arrow), with clockwise rotation of the analyzer defined as positive. The six spectra in **Fig. 3a** represent the  ${}^5D_0 \rightarrow {}^7F_1$  magnetic dipole (MD) transition of  $Eu^{3+}$  dopants measured under six polarization bases by the PS method. In hexagonal  $YPO_4:Eu^{3+}$  crystal,  $Y^{3+}$  ions occupy crystallographic sites with  $D_2$  point group symmetry<sup>72</sup>. If  $Eu^{3+}$  ions substitute at these sites maintaining the same symmetry, the  ${}^5D_0 \rightarrow {}^7F_J$  ( $J = 0, 1, 2, 3, 4$ ) transitions exhibit 1, 3, 5, 7, and 9 splitting peaks, respectively<sup>12,43</sup>. Due to strong electron-phonon-photon coupling at room temperature<sup>75-78</sup>, splitting for  $J > 1$  quantum states are indistinguishable (**Supplementary Section III Fig. 8**). While the  $J = 0$  transition exhibits only one peak, its inherent characteristic of forbidden transition result in extremely low luminescence intensity<sup>12</sup>. Therefore, we focus on the strong  ${}^5D_0 \rightarrow {}^7F_1$  magnetic dipole transition, performing quantitative polarization spectroscopy on the three resolvable emission peaks to determine the corresponding magnetic dipole orientations. Using the PS method, we plotted the  $S_1$ ,  $S_2$ , and  $S_3$  of the transition in **Fig. 3b**.  $S_3$  approaches zero, with only minor fluctuations less than 0.1 near 597 nm, possibly indicating the right-handed optical activity. Overall,  $S_3 = 0$  ensures that dipole emission remains unmodulated by the crystal during propagation, thereby guaranteeing the

accuracy of dipole orientation determination. In contrast to the  $S_3$ ,  $S_1$  and  $S_2$  exhibit opposite values between the spectral ranges of 579-591 nm and 591-603 nm, indicating orthogonal linear polarization. **Fig. 3c** shows the transition fitted well with the three Lorentzian peaks. Using the integrated intensities, we determined the  $(S_1, S_2, S_3)$  for peaks I, II, and III as  $(-0.38, 0.41, 0.02)$ ,  $(-0.06, 0.05, -0.01)$ , and  $(0.49, -0.63, 0.08)$ , respectively, which almost lie within the equatorial plane of Poincaré sphere, as illustrated in **Fig. 3d**. Notably, peak III exhibits a larger  $S_3$  compared to peaks I and II, demonstrating right-handed chirality of this single microcrystal. From  $S_1$  and  $S_2$ , the linear polarization angles  $\Omega$  of the three emission peaks are  $66.3^\circ$ ,  $70.2^\circ$ , and  $154.0^\circ$ , with linear polarization degrees LDOPs of 0.55, 0.07, and 0.80, respectively (**Supplementary Section III Table 3 for sample no. 1**). Peaks I and II exhibit polarization angles perpendicular to the crystal  $c$ -axis ( $\Omega = \Omega_c - \pi/2$ ), while peak III is parallel to the  $c$ -axis ( $\Omega = \Omega_c$ ). This agreement with theoretical predictions validates both the single-particle dipoles emission model and the computational electromagnetics approach. Given the near-zero  $S_3$  value, we analyzed the polarization using the PF method, as shown in **Figs 3e,f**. The polarization fitting yielded linear polarization angles  $\Omega$  of  $66.4^\circ$ ,  $66.4^\circ$ , and  $156.4^\circ$  and degrees LDOPs of 0.54, 0.08, and 0.77 for the three peaks, respectively (**Supplementary Section III Table 4 for sample no. 1**). The results obtained from the PF method are in close agreement with those derived from the PS approach, demonstrating that they are both valid for extracting the polarization information in the situation of  $S_3 = 0$ .

To further support our polarization conclusions, we measured another nine microcrystals of the same crystalline structure with different in-plane orientations (**Supplementary Section III Figs 9,10**). These samples show exactly the same partial linear polarization features with the small standard deviations of LDOPs ( $< 0.05$ ), confirming the robustness of our experimental conclusions. (**Supplementary Section III Tables 3,4 for sample nos 2-10**). Furthermore, we checked the  $S_3$  values of the peak III in the ten single microcrystals, as shown in **Fig. 3g**. Interestingly, six microcrystals display  $S_3 > 0$  (four with  $S_3 < 0$ ), corresponding to right- (left-) handed optical activity, with an average  $S_3 = 0$ , suggesting an external racemic property of single-particle ensembles. We experimentally confirmed the racemic nature and unpolarized emission from a random single-particle ensemble, as illustrated in **Figs 3h,i**. The hexagonal  $\text{YPO}_4$  crystallizes in the  $P6_222$  chiral space group<sup>71-74,79</sup>. The statistical consistency of left- and right- handed single microcrystals, coupled with the racemic nature of the ensemble, indicates spontaneous chiral symmetry breaking during crystallization.

**Transition dipole orientation analysis.** To determine the dipole orientation, we assume  $\alpha_I$ ,  $\alpha_{II}$ , and  $\alpha_{III}$  as the magnetic dipole orientation angles corresponding to the three emission peaks, as illustrated in **Fig. 4a**. From the polarization conclusions, the linear polarization angles of the peaks I and II are perpendicular to the crystal c-axis, enabling the calculation of  $\alpha_I$  and  $\alpha_{II}$  using **Eq. 9**. Conversely, the polarization angle of the peak III aligns parallel to the c-axis, allowing the determination of  $\alpha_{III}$  through **Eq. 8**. Using the LDOPs, we calculated the dipole orientations of the three peaks in the ten single microcrystals (**Supplementary Section III Tables 3,4**). Remarkably, both the PS and PF methods yield identical averages with negligibly small standard deviations, further validating their efficacy. The left of **Fig. 4b** displays the distribution of the magnetic dipole orientations derived from the PF method. The mean values were determined to be  $37.6^\circ$ ,  $52.8^\circ$ , and  $75.3^\circ$  for  $\alpha_I$ ,  $\alpha_{II}$ , and  $\alpha_{III}$ , respectively, with all standard deviations less than  $1.5^\circ$ . If the  $\text{Eu}^{3+}$  ion occupy the  $D_2$  point group symmetry<sup>72</sup>, the selection rules for the  $^5D_0 \rightarrow ^7F_1$  magnetic optical transition dictate (**Supplementary Section III Table 1**)<sup>11,46</sup>: (1) the presence of three splitting peaks (consistent with our experimental observations), and (2) the three types of magnetic transition dipole  $R_X$ ,  $R_Y$ , and  $R_Z$  corresponding to the three peaks are expected to be mutually orthogonal, thus satisfying a specific mathematical relation:

$$\cos \alpha_I + \cos \alpha_{II} + \cos \alpha_{III} = 1 \quad (10)$$

or

$$\cos \alpha_I = 1 - \cos \alpha_{II} - \cos \alpha_{III} \quad (11)$$

$$\cos \alpha_{II} = 1 - \cos \alpha_I - \cos \alpha_{III} \quad (12)$$

$$\cos \alpha_{III} = 1 - \cos \alpha_I - \cos \alpha_{II} \quad (13)$$

Considering the significant linear polarization degree and minimal standard deviation observed for peaks I and III, we substituted the  $\alpha_I$  and  $\alpha_{III}$  values derived from the PF method into **Eq. 12** to calculate the theoretical transition angle  $\alpha_{II}$  for the magnetic dipole II in the ten individual microcrystals (**Supplementary Section III Table 5**). The statistical results are plotted in the right of **Fig. 4b**. The theoretically mean value  $\alpha_{II}$  of  $56.3^\circ$  differs from the experimentally obtained average of  $52.8^\circ$  by only  $3.5^\circ$ , demonstrating the orthogonal geometric relationship among the three magnetic transition dipoles. The minor discrepancy may arise from the optical chirality of the crystal at peak III and the limitations in the objective lens numerical aperture for collecting non-radial emission from single particles, aspects requiring further optimization of sample selection and experimental methodology. Notably, the theoretical transition angle of  $56.3^\circ$  for magnetic dipole II, which is

approximately the same value as the unpolarized transition dipole derived by computational electromagnetics (54.7°, see **Fig. 2c**), explains the minimal linear polarization degree (LDOP = 0.08) observed for the peak II. The dipole orientation analysis demonstrates that Eu<sup>3+</sup> ions are situated within, or extremely close to, the D<sub>2</sub> point group symmetry in the hexagonal YPO<sub>4</sub> microcrystals. Such a symmetry features three mutually orthogonal C<sub>2</sub> symmetry axes (X, Y, and Z)<sup>11,46</sup>, corresponding to the orientations (37.6°, 52.8°, and 75.3°) of the three magnetic transition dipoles, respectively.

Unlike the conventional method for determining point group symmetry, which relies on counting transition splittings in bulk or powdered samples at cryogenic temperatures, this study presents a comprehensive theoretical and experimental approach to determining local point group symmetry (quantum system symmetry) by resolving the optical transition dipole orientations of single-particle emitters using room-temperature polarized spectroscopy. This method offers unparalleled advantages, particularly when the transition splitting numbers are identical. For instance, in hexagonal YPO<sub>4</sub> crystals, a symmetry breakdown from D<sub>2</sub> to C<sub>2</sub> would still yield three magnetic dipole emission peaks<sup>43</sup>. However, the dipole orientations would not exhibit the required orthogonality (**Supplementary Section III Table 2**). Importantly, our approach directly resolves the symmetry axes orientation of the point group, a capability unattainable by the conventional spectroscopic method and advanced crystallographic characterization techniques such as X-ray diffraction (XRD) or scanning transmission electron microscopy (STEM). This has significant implications for characterizing local symmetry features (< 1 nm<sup>3</sup>), especially vectorial symmetries in materials.

**3D orientation sensing by transition bands.** Beyond probing point group symmetry, our approach enables extracting three-dimensional (3D) orientation of single particles through polarized spectroscopy. As previously demonstrated, the magnetic dipole emission satisfies the partial linear polarization **Eq. 7** along the radial directions of the single-particle crystals. Consequently, the polarization-resolved intensity for an arbitrary magnetic transition band (comprising multiple magnetic dipole emission peaks) can be expressed as:

$$I'_{\omega} = \sum I_{i\parallel} \cos^2(\omega - \Omega_c) + \sum I_{i\perp} \sin^2(\omega - \Omega_c) = I'_{\parallel} \cos^2(\omega - \Omega_c) + I'_{\perp} \sin^2(\omega - \Omega_c) \quad (14)$$

Here,  $i$  indexes the  $i$ th emission peak within the band. Clearly, any such transition band exhibits partial linear polarization. For  $I'_{\parallel} > I'_{\perp}$ , the linear polarization angle aligns with the crystal c-axis, yielding LDOP =  $(I'_{\parallel} - I'_{\perp}) / (I'_{\parallel} + I'_{\perp})$ . Conversely, when  $I'_{\parallel} < I'_{\perp}$ , the polarization angle is perpendicular to the c-axis, resulting in LDOP =  $(I'_{\perp} - I'_{\parallel}) / (I'_{\parallel} + I'_{\perp})$ . We tested this hypothesis by resolving the  ${}^5D_0 \rightarrow {}^7F_1$

magnetic transition of the single microcrystal (sample no. 1) into two transition bands I and II (**Fig. 5a–c**). The PS analysis of the integrated intensities demonstrated that both two bands display partial linear polarization, with their coordinates located within the equatorial plane of Poincaré sphere (**Fig. 5d**). Specifically, band I exhibits a linear polarization angle of  $66.6^\circ$ , perpendicular to the crystal c-axis, while band II shows a polarization angle of  $155.6^\circ$ , aligned parallel to the c-axis (**Supplementary Section IV Table 6 for sample no. 1**). Moreover, statistical analysis demonstrates remarkable consistency in the LDOPs across ten single microcrystals (**Fig. 5e**), with a standard deviation less than 0.02 (**Supplementary Section IV Table 6**). This robust polarization characteristic is crucial for spatially resolving single-particle orientations.

**Fig. 5f** depicts the orthogonally linear polarization detection scheme for determining the 3D orientation of a single particle. It is performed in a  $x'$ - $y'$ - $z'$  Cartesian coordinate system, where  $\theta'$  and  $\varphi'$  represent the polar and azimuthal angles, respectively, and  $I_{z'x'}$  and  $I_{z'y'}$  are the orthogonally detected intensities along  $z'$  direction. In one of our previous works<sup>47</sup>, we established a method to determine the 3D orientation of a rare-earth-doped single particle using any two emission peaks. However, this approach requires Lorentzian spectral fitting to resolve individual peaks, which can be difficult for many rare-earth-doped crystals at room temperature due to the wide linewidth of multi-dipoles affected by phonons. In contrast, herein we employ integrated transition bands instead of individual peaks, which overcomes the resolution limitation associated with single-peak linewidth, and thereby provides a more practical and accessible approach. The analytical expressions for a single-particle 3D orientation based on two magnetic transition bands are provided as (**Supplementary Section IV Fig. 11**):

$$\sin^2\theta' = \frac{\left(\frac{I_{2z'y'}}{I_{2z'x'}} - C_2\right)(1-C_1) - \left(\frac{I_{1z'y'}}{I_{1z'x'}} - C_1\right)(1-C_2)}{\left(\frac{I_{2z'y'}}{I_{2z'x'}} - \frac{I_{1z'y'}}{I_{1z'x'}}\right)(C_1-1)(C_2-1)} \quad (15)$$

$$\sin^2\varphi' = \frac{\frac{I_{1z'y'}}{I_{1z'x'}}[\sin^2\theta'(C_1-1)+1] - C_1}{\sin^2\theta'(1-C_1)} \quad (16)$$

or

$$\sin^2\varphi' = \frac{\frac{I_{2z'y'}}{I_{2z'x'}}[\sin^2\theta'(C_2-1)+1] - C_2}{\sin^2\theta'(1-C_2)} \quad (17)$$

Here, subscripts 1 and 2 refer to the two selected magnetic transition bands, the

parameters  $C_1$  and  $C_2$  are defined as the ratios  $I'_{1\parallel}/I'_{1\perp}$  and  $I'_{2\parallel}/I'_{2\perp}$ , respectively. With the LDOPs of the transition bands I and II defined by  $LDOP_1 = (I'_{1\perp} - I'_{1\parallel})/(I'_{1\parallel} + I'_{1\perp})$  (the linear polarization angle being perpendicular to the c-axis) and  $LDOP_2 = (I'_{2\parallel} - I'_{2\perp})/(I'_{2\parallel} + I'_{2\perp})$  (parallel to the c-axis), respectively,  $C_1$  and  $C_2$  are derived as:

$$C_1 = \frac{1-LDOP_1}{1+LDOP_1} \quad (18)$$

$$C_2 = \frac{1+LDOP_2}{1-LDOP_2} \quad (19)$$

Combining **Eqs. 15-18**, we can obtain the 3D orientation information of a single particle through the single-view angle polarization measurements and the transition band LDOPs. Beyond the hexagonal  $YPO_4:Eu^{3+}$  single particles, this optical sensing method is applicable to any rare-earth-doped single-particle crystals with rotational symmetry (e.g., hexagonal  $NaYF_4:Yb^{3+},Er^{3+},Ho^{3+},Tm^{3+},Nd^{3+},Pr^{3+}$ )<sup>80</sup>. The robust polarization fluorescence stemming from oriented dipoles emission allows the rare-earth-doped single particles to function as “individual microscopic antennas”, enabling spectroscopic sensing of rotational dynamics at the micro- and nanoscale, such as the rotation of DNA, macromolecules, proteins, and subcellular organelles within single cells<sup>81</sup>.

## Conclusion

Through computational electromagnetics, we provided the rigorous analysis of far-field polarized emission from the rare-earth-doped single-particle crystal, deriving a quantitative relationship between rare-earth ion magnetic transition dipole orientation and single-particle far-field polarization intensity. By combining high-precision polarization-resolved spectroscopy of single particles at room-temperature, we quantitatively calculated the three dipole orientations from one magnetic optical transition, demonstrating the point group symmetry of rare-earth ions within single microcrystals and obtaining the vectorial symmetry information — a feat unachievable by traditional low-temperature spectroscopy and existing crystallographic characterization techniques.

Furthermore, we discovered the chiroptical activity of the single particles, originating from spontaneous symmetry breaking within the intrinsic chiral space group during crystallization. Based on the robust polarized luminescence of rare-earth-doped single particles, we proposed a practical spectroscopy sensing approach that utilizes any two optical transition bands from single-view polarization spectra to discriminate the 3D orientation of single micro- and nanocrystals.

The computational electromagnetic analysis introduced in this study not only enables quantitative understanding of the polarized luminescence from rare-earth-doped single crystals, but also provides a framework for analyzing and predicting the extreme polarization phenomena associated with electromagnetic dipoles coherent radiation, such as amplified stimulated emission (ASE), superradiance (SR), and superfluorescence<sup>69</sup> (SF) in single emitters.

## References:

1. Yang, C. N. Symmetry and Physics. In *The Oskar Klein Memorial Lectures*, Vol. 1 (ed. Ekspong, G.) 11–33 (World Scientific, 1991).
2. Yang, C. N. Einstein's impact on theoretical physics. *Phys. Today* **33**, 42–49 (1980).
3. Einstein, A. Zur Elektrodynamik bewegter Körper. *Annalen der Physik* **322**, 891–921 (1905).
4. Misner, C. W., Thorne, K. S. & Wheeler, J. A. *Gravitation*. (W. H. Freeman, 1973).
5. Shankar, R. *Principles of Quantum Mechanics*. (Springer, 1994).
6. Peskin, M. E. & Schroeder, D. V. *An Introduction to Quantum Field Theory*. (Westview Press, 1995).
7. Hammond, C. *The Basics of Crystallography and Diffraction* (Oxford University Press, 2009).
8. Powell, R. C. *Symmetry, Group Theory, and the Physical Properties of Crystals*. (Springer, 2010).
9. Henderson, B. & Imbusch, G. F. *Optical Spectroscopy of Inorganic Solids*. (Clarendon Press, 1989).
10. Stoneham, A. M. *Theory of Defects in Solids*. (Clarendon Press, 1985).
11. Görller-Walrand, C. & Binnemans, K. In *Handbook on the Physics and Chemistry of Rare Earths* Vol. 23, 121 (Elsevier, 1996).
12. Binnemans, K. Interpretation of europium(III) spectra. *Coord. Chem. Rev.* **295**, 1–45 (2015).
13. Walsh, B. M. *Judd-Ofelt Theory: Principles and Practices*. NASA Langley Research Center, Hampton, VA. Vol. 231, 403–433 (2006).
14. Wigner, E. *Gruppentheorie und ihre Anwendung auf die Quantenmechanik der Atomspektren* (Braunschweig, 1931).
15. Wang, F. *et al.* Simultaneous phase and size control of upconversion nanocrystals through lanthanide doping. *Nature* **463**, 1061–1065 (2010).
16. Zhao, J. *et al.* Single-nanocrystal sensitivity achieved by enhanced upconversion luminescence. *Nat. Nanotechnol.* **8**, 729–734 (2013).
17. Deng, R. *et al.* Temporal full-colour tuning through non-steady-state upconversion. *Nat. Nanotechnol.* **10**, 237–242 (2015).
18. Zhou, B., Shi, B., Jin, D. & Liu, X. Controlling upconversion nanocrystals for emerging applications. *Nat. Nanotechnol.* **10**, 924–936 (2015).
19. Fernandez-Bravo, A. *et al.* Continuous-wave upconverting nanoparticle microlasers. *Nat.*



- Nanotechnol.* **13**, 572–577 (2018).
20. Fernandez-Bravo, A. *et al.* Ultralow-threshold, continuous-wave upconverting lasing from subwavelength plasmons. *Nat. Mater.* **18**, 1172–1176 (2019).
  21. Liang, F. *et al.* Multiphonon-assisted lasing beyond the fluorescence spectrum. *Nat. Phys.* **18**, 1312–1316 (2022).
  22. Liu, Y. *et al.* Amplified stimulated emission in upconversion nanoparticles for super-resolution nanoscopy. *Nature* **543**, 229–233 (2017).
  23. Liu, Q. *et al.* Single upconversion nanoparticle imaging at sub-10 W cm<sup>-2</sup> irradiance. *Nat. Photonics* **12**, 548–553 (2018).
  24. Ou, X. *et al.* High-resolution X-ray luminescence extension imaging. *Nature* **590**, 410–415 (2021).
  25. Pei, P. *et al.* X-ray-activated persistent luminescence nanomaterials for NIR-II imaging. *Nat. Nanotechnol.* **16**, 1011–1018 (2021).
  26. Lee, C. *et al.* Giant nonlinear optical responses from photon-avalanching nanoparticles. *Nature* **589**, 230–235 (2021).
  27. Lee, C. *et al.* Indefinite and bidirectional near-infrared nanocrystal photoswitching. *Nature* **618**, 951–958 (2023).
  28. Liang, Y. *et al.* Migrating photon avalanche in different emitters at the nanoscale enables 46th-order optical nonlinearity. *Nat. Nanotechnol.* **17**, 524–530 (2022).
  29. Fardian-Melamed, N. *et al.* Infrared nanosensors of piconewton to micronewton forces. *Nature* **637**, 70–75 (2025).
  30. Casar, J. R. *et al.* Upconverting microgauges reveal intraluminal force dynamics in vivo. *Nature* **637**, 76–83 (2025).
  31. Shan, X. *et al.* Sub-femtonewton force sensing in solution by super-resolved photonic force microscopy. *Nat. Photon.* **18**, 913–921 (2024).
  32. Kim, J. *et al.* Monitoring the orientation of rare-earth-doped nanorods for flow shear tomography. *Nat. Nanotechnol.* **12**, 914 (2017).
  33. Kim, J. *et al.* Measuring 3D orientation of nanocrystals via polarized luminescence of rare-earth dopants. *Nat. Commun.* **12**, 1943 (2021).
  34. Wang, Z. *et al.* Shearometry of fluids with tunable rheology by polarized luminescence of rare earth-doped nanorods. *ACS Nano* **18**, 30650–30657 (2024)

35. Kindem, J. M. *et al.* Control and single-shot readout of an ion embedded in a nanophotonic cavity. *Nature* **580**, 201–204 (2020).
36. Serrano, D. *et al.* Ultra-narrow optical linewidths in rare-earth molecular crystals. *Nature* **603**, 241–246 (2022).
37. Schiattarella, C. *et al.* Directive giant upconversion by supercritical bound states in the continuum. *Nature* **626**, 765–771 (2024).
38. Ding, D. *et al.* Multidimensional Purcell effect in an ytterbium-doped ring resonator. *Nat. Photonics* **10**, 385–388 (2016).
39. Yang, L. *et al.* Controlling single rare earth ion emission in an electro-optical nanocavity. *Nat. Commun.* **14**, 1718 (2023).
40. Meng, Y. *et al.* Bright single-nanocrystal upconversion at sub 0.5 W cm<sup>-2</sup> irradiance via coupling to single nanocavity mode. *Nat. Photonics* **17**, 73–81 (2023).
41. Chen, H. *et al.* Sub-50-ns ultrafast upconversion luminescence of a rare-earth-doped nanoparticle. *Nat. Photonics* **16**, 651–657 (2022).
42. Aebischer, A. *et al.* Structural and spectroscopic characterization of active sites in a family of light-emitting sodium lanthanide tetrafluorides. *Angew. Chem. Int. Ed.* **45**, 2802–2806 (2006).
43. Liu, Y., Tu, D., Zhu, H. & Chen, X. Lanthanide-doped luminescent nanoprobes: controlled synthesis, optical spectroscopy, and bioapplications. *Chem. Soc. Rev.* **42**, 6924–6958 (2013).
44. Tu, D. *et al.* Breakdown of Crystallographic Site Symmetry in Lanthanide-Doped NaYF<sub>4</sub> Crystals. *Angew. Chem.* **125**, 1166–1171 (2013).
45. Nielsen, V. R. M., Guennic, B. L. & Sørensen, T. J. Evaluation of Point Group Symmetry in Lanthanide(III) Complexes: A New Implementation of a Continuous Symmetry Operation Measure with Autonomous Assignment of the Principal Axis. *J. Phys. Chem. A* **128**, 5740–5751 (2024).
46. Atkins, P. W., Child, M. S. & Phillips, C. S. G. *Tables for Group Theory*. Oxford University Press, Oxford (1970).
47. Li, P. *et al.* Deterministic Relation between Optical Polarization and Lattice Symmetry Revealed in Ion-Doped Single Microcrystals. *ACS Nano* **16**, 9535–9545 (2022).
48. Sayre, E. V., Sancier, K. M. & Freed, S. Absorption spectrum and quantum states of the praseodymium ion. I. Single crystals of praseodymium chloride. *J. Chem. Phys.* **23**, 2060–2065

(1955).

49. Sayre, E. V. & Freed, S. Absorption spectrum and quantum states of the praseodymium ion. II. anhydrous praseodymium fluoride in films. *J. Chem. Phys.* **23**, 2066–2068 (1955).
50. Sayre, E. V. & Freed, S. Spectra and quantum states of the europic ion in crystals. I. absorption spectrum of anhydrous europic chloride. *J. Chem. Phys.* **24**, 1211–1212 (1956).
51. Sayre, E. V. & Freed, S. Spectra and quantum states of the europic ion in crystals. II. fluorescence and absorption spectra of single crystals of europic ethylsulfate nonahydrate. *J. Chem. Phys.* **24**, 1213–1219 (1956).
52. Blanc, J. & Ross, D. L. Polarized absorption and emission in an octacoordinate chelate of  $\text{Eu}^{3+}$ . *J. Chem. Phys.* **43**, 1286–1289 (1965).
53. Brecher, C. *et al.* Polarized spectra and crystal-field parameters of  $\text{Eu}^{3+}$  in  $\text{YVO}_4$ . *Phys. Rev.* **155**, 178 (1967).
54. Brecher, C. *et al.* Polarized spectra and crystal-field parameters of  $\text{Eu}^{3+}$  in  $\text{YPO}_4$ . *J. Chem. Phys.* **49**, 3303–3311 (1968).
55. Brecher, C. Europium in the ultraphosphate lattice: polarized spectra and structure of  $\text{EuP}_5\text{O}_{14}$ . *J. Chem. Phys.* **61**, 2297–2315 (1974).
56. Zhou, J., Chizhik, A. I., Chu, S. & Jin, D. Single-particle spectroscopy for functional nanomaterials. *Nature* **579**, 41–50 (2020).
57. Zhou, J. *et al.* Ultrasensitive polarized up-conversion of  $\text{Tm}^{3+}$ - $\text{Yb}^{3+}$  doped  $\beta$ - $\text{NaYF}_4$  single nanorod. *Nano Lett.* **13**, 2241–2246 (2013).
58. Rodríguez-Sevilla, P. *et al.* Determining the 3D orientation of optically trapped upconverting nanorods by in situ single-particle polarized spectroscopy. *Nanoscale* **8**, 300–308 (2016).
59. Green, K. K., Wirth, J. & Lim, S. F. Nanoplasmonic upconverting nanoparticles as orientation sensors for single particle microscopy. *Sci. Rep.* **7**, 762 (2017).
60. Yang, D. *et al.* Anisotropic excitation polarization response from a single white light-emitting  $\beta$ - $\text{NaYF}_4:\text{Yb}^{3+},\text{Pr}^{3+}$  microcrystal. *Small* **15**, 1904298 (2019).
61. Li, P. *et al.* Orthogonally polarized luminescence of single bismuth phosphate microcrystal doped with europium. *Adv. Optical Mater.* **8**, 2000583 (2020).
62. Chacon, R. *et al.* Measuring the magnetic dipole transition of single nanorods by spectroscopy and Fourier microscopy. *Phys. Rev. Appl.* **14**, 054010 (2020).

63. Lyu, Z.-Y., Dong, H., Yang, X.-F., Sun, L.-D. & Yan, C.-H. Highly polarized upconversion emissions from lanthanide-doped LiYF<sub>4</sub> crystals as spatial orientation indicators. *J. Phys. Chem. Lett.* **12**, 11288–11294 (2021).
64. Wei, S. *et al.* Polarized upconversion luminescence from a single LiLuF<sub>4</sub>:Yb<sup>3+</sup>/Er<sup>3+</sup> microcrystal for orientation tracking. *Sci. China Mater.* **65**, 220–228 (2022).
65. Wen, D. *et al.* Tunable excitation polarized upconversion luminescence and reconfigurable double anti-counterfeiting from Er<sup>3+</sup> doped single nanorods. *Adv. Opt. Mater.* **11**, 2301126 (2023).
66. Cai, Y., Shang, Y., Lu, M., Jin, D. & Zhou, J. Polarized upconversion of sub-100 nm single nanoparticles. *Nano Lett.* **24**, 10915–10920 (2024).
67. Förster, T. Energiewanderung und Fluoreszenz. *Naturwissenschaften* **33**, 166–175 (1946).
68. Szabó, Á., Szöllosi, J. & Nagy, P. Principles of resonance energy transfer. *Curr. Protoc.* **2**, e625 (2022).
69. Huang, K. *et al.* Room-temperature upconverted superfluorescence. *Nat. Photon.* **16**, 737–742 (2022).
70. Hikichi, Y. *et al.* Mechanochemical Changes of Weinschenkite-Type RPO<sub>4</sub>·2H<sub>2</sub>O (R = Dy, Y, Er, or Yb) by Grinding and Thermal Reactions of the Ground Specimens. *J. Am. Ceram. Soc.* **12**, 1073-1076 (1989).
71. Mooney, R. C. L. X-ray Diffraction Study of Cerous Phosphate and Related Crystals. I. Hexagonal Modification. *Acta Crystallogr.* **3**, 337 (1950).
72. Ma, C.-G. *et al.* Vacuum ultraviolet spectroscopic analysis of Ce<sup>3+</sup>-doped hexagonal YPO<sub>4</sub>·0.8H<sub>2</sub>O based on exchange charge model. *J. Lumin.* **152**, 70-74 (2014).
73. Vanetsev, A. S. *et al.* Phase composition and morphology of nanoparticles of yttrium orthophosphates synthesized by microwave-hydrothermal treatment: The influence of synthetic conditions. *J. Alloys Compd.* **639**, 415-421 (2015).
74. Li, P. *et al.* Phase Control of Eu<sup>3+</sup>-Doped YPO<sub>4</sub> Nano-/Microcrystals. *Cryst. Growth Des.* **17**, 5935-5944 (2017).
75. Luwang, M. N. *et al.* Effects of Ce<sup>3+</sup> Codoping and Annealing on Phase Transformation and Luminescence of Eu<sup>3+</sup>-Doped YPO<sub>4</sub> Nanorods: D<sub>2</sub>O Solvent Effect. *J. Am. Chem. Soc.* **132**, 2759-2768 (2010).
76. Luwang, M. N. *et al.* Disappearance and Recovery of Luminescence in Bi<sup>3+</sup>, Eu<sup>3+</sup> Codoped YPO<sub>4</sub>

- Nanoparticles Due to the Presence of Water Molecules up to 800 °C. *J. Am. Chem. Soc.* **133**, 2998-3004 (2011).
77. Mishra, S. K. *et al.* Neutron diffraction reveals the existence of confined water in triangular and hexagonal channels of modified YPO<sub>4</sub> at elevated temperatures. *Phys. Rev. Mater.* **1**, 046002 (2017).
78. Mishra, S. K. *et al.* Presence of water at elevated temperatures, structural transition, and thermal expansion behavior in LaPO<sub>4</sub>:Eu. *Phys. Rev. Mater.* **2**, 126003 (2018).
79. Fu, W., Tan, L. & Wang, P. Chiral Inorganic Nanomaterials for Photo(electro)catalytic Conversion. *ACS Nano* **17**, 16326-16347 (2023).
80. Zheng, B. *et al.* Rare-Earth Doping in Nanostructured Inorganic Materials. *Chem. Rev.* **122**, 5519-5603 (2022).
81. Yang, Z. *et al.* Biological Applications of Fluorescence Polarization Imaging. *Laser Optoelectron. Prog.* **61**, 1800001 (2024).
82. Freeman, R., King, J. & Lafyatis, G. *Electromagnetic Radiation* (Oxford University Press, 2019).

## Methods

**Sample preparation and characterization.** We synthesized hexagonal  $\text{YPO}_4:\text{Eu}^{3+}$  single microcrystals via a hydrothermal method. First, 910 mg of yttrium nitrate hexahydrate ( $\text{Y}(\text{NO}_3)_3 \cdot 6\text{H}_2\text{O}$ ) and 56 mg of europium nitrate hexahydrate ( $\text{Eu}(\text{NO}_3)_3 \cdot 6\text{H}_2\text{O}$ ) were dissolved in 15 mL of deionized water and thoroughly mixed using magnetic stirring. Subsequently, 2385 mg of  $\text{Na}_2\text{CO}_3$  and 288 mg of  $\text{NH}_4\text{H}_2\text{PO}_4$  were individually dissolved in separate 15 mL of deionized water. The  $\text{Na}_2\text{CO}_3$  solution was then slowly added to the initial mixed solution, followed by 30 minutes of magnetic stirring. The  $\text{NH}_4\text{H}_2\text{PO}_4$  solution was subsequently added dropwise to the mixture. After continuous stirring for 1 hour, the mixture was transferred to a stainless-steel autoclave equipped with a polytetrafluoroethylene (PTFE) liner and heated at  $180^\circ\text{C}$  for 9 hours. Upon natural cooling to room temperature, the white precipitate was repeatedly washed and centrifuged using deionized water and anhydrous ethanol. The sample was then dried at  $80^\circ\text{C}$  for 12 hours, yielding a white powder product. The powder structure characterization was performed using X-ray diffraction (XRD, Rigaku D/Max2550, 40 kV, 50 mA,  $\text{Cu K}\alpha$ ,  $\lambda = 1.5406 \text{ \AA}$ ) with a  $2\theta$  scanning range of  $10^\circ$ - $60^\circ$  and a scan rate of  $8^\circ/\text{min}$  (**Supplementary Section I Fig. 1a**). Morphological analysis was conducted using scanning electron microscopy (SEM, Hitachi S-4800, 3 kV) (**Supplementary Section I Fig. 1b**). To visualize the spatial distribution of  $\text{Y}^{3+}$  ions in the hexagonal  $\text{YPO}_4$  crystal, we generated the unit cell structure using VESTA software (**Fig. 1a**). For single-particle luminescence characterization, the powder sample was dissolved in ethanol and dispersed on a quartz substrate, forming a randomly in-plane distribution of single microcrystals (**Fig. 3a**, and **Supplementary Section III Figs 9**) and their ensembles (**Fig. 3h**).

**Far-field polarized analysis.** Using the far-field radiation formula of a single oscillating magnetic dipole (**Eq. 20**)<sup>82</sup>, we calculated the far-field polarization intensity for an arbitrary single transition magnetic dipole by employing the commercial computational software Mathematica (**Supplementary Section II Fig. 2**). The sixfold rotational symmetry of the magnetic dipoles in the single microcrystals allowed us to determine the total far-field polarization intensity by incoherent superposition of the intensities from six dipoles (**Supplementary Section II Fig. 3**).

$$\vec{E}(\vec{r}, t) = \frac{\mu_0 m_0 c k^2}{4\pi r} e^{j(\omega t - kr)} (\hat{r} \times \hat{m}) \quad (20)$$

where  $\mu_0$ ,  $m_0$ ,  $c$ ,  $k$ ,  $\omega$ , and  $r$  are the vacuum permeability, maximum magnetic dipole moment, speed of light, wave vector, oscillation frequency, and distance from the dipole to the field point, respectively,

and  $\hat{\mathbf{r}}$  and  $\hat{\mathbf{m}}$  are the unit vectors of the field point and magnetic dipole, respectively. To achieve 3D orientation resolution of a single particle, we applied a coordinate transformation to the six magnetic dipoles. By substituting the transformed unit vectors  $\bar{\mathbf{R}}\hat{\mathbf{m}}_{i=1,\dots,6}$  (where  $\bar{\mathbf{R}}$  is the transformation matrix) into **Eq. 20**, we analytically derived the orthogonal linear polarized intensities for any 3D orientation of the single particle (**Supplementary Section IV Fig. 11**).

**Single-particle polarized measurements.** To quantitatively investigate the polarized luminescence properties of single particles, we constructed a high-precision polarization-resolved microspectroscopy system (**Supplementary Section III Fig. 6**). On the excitation light path, we generated a 395 nm pure linearly polarized beam using a titanium-sapphire femtosecond laser and second-harmonic generation (SHG) optical path. This wavelength effectively excites  $\text{Eu}^{3+}$  ions to the  $^5\text{L}_6$  excited state, inducing fluorescence emission from the  $\text{YPO}_4:\text{Eu}^{3+}$  single particles. To eliminate potential polarization effects of the excitation light on single-particle polarized luminescence, we converted the pure linear polarization to circular polarization using a half-wave plate (10RP02-48, Newport) and a quarter-wave plate (10RP04-48, Newport). In fact, due to the crystal phonon depolarization mechanism, the polarization state of non-resonant excitation does not affect the polarized luminescence characteristics of rare-earth dopants. The 395 nm laser beam, after passing through a non-polarizing beam splitter (BS), was focused onto single particles on a quartz substrate using a low numerical aperture microscope objective (NA = 0.55, M Plan Apo 100x, Mitutoyo). The substrate, mounted on a three-axis nanopositioning stage, enables movement and scanning in x-y-z directions. In the collection light path, fluorescence signal and scattered excitation light from single particles pass through the microscope objective and enter a non-polarizing beam splitter. A long-pass dichroic mirror (405 nm, FL-007036, Semrock) filters out the background scattering, allowing only the fluorescence signal to enter the detection light path. This enables in-plane orientation analysis (CCD) and spectral polarization resolution of single particles. To achieve polarization resolution, fluorescence pass through a rotatable half-wave plate (10RP52-1B, Newport) or quarter-wave plate (10RP54-1B, Newport) and a linear polarizer (WP25M-VIS, Thorlabs), ultimately focusing on a spectrometer (Shamrock SR-750-A, Andor) equipped with an EMCCD camera (DU970P-BVF, Andor). To eliminate polarization effects from the spectrometer grating orientation, we fixed the linear polarizer orientation parallel to the spectrometer slit direction (defined as  $0^\circ$ ), recording spectral changes only

by rotating the half-wave or quarter-wave plate. For two polarization analysis methods, the polarization Poincaré sphere (PS) method requires measuring six polarization basis vectors  $I(0^\circ)$ ,  $I(90^\circ)$ ,  $I(45^\circ)$ ,  $I(-45^\circ)$ ,  $I(\sigma^+)$ , and  $I(\sigma^-)$ . These correspond to rotating the half-wave plate long axis to  $0^\circ$ ,  $45^\circ$ ,  $22.5^\circ$ ,  $-22.5^\circ$  ( $337.5^\circ$ ), and the quarter-wave plate long axis to  $45^\circ$  and  $-45^\circ$  ( $315^\circ$ ), respectively. Based on the six polarization vectors, we obtain the three normalized Stokes parameters ( $S_1$ ,  $S_2$ ,  $S_3$ ) for describing the luminescence polarization state.

$$S_1 = \frac{I(0^\circ) - I(90^\circ)}{I(0^\circ) + I(90^\circ)} \quad (21)$$

$$S_2 = \frac{I(45^\circ) - I(-45^\circ)}{I(45^\circ) + I(-45^\circ)} \quad (22)$$

$$S_3 = \frac{I(\sigma^+) - I(\sigma^-)}{I(\sigma^+) + I(\sigma^-)} \quad (23)$$

However, the polarization fitting (PF) method requires linearly polarized measurements every  $15^\circ$  from  $0^\circ$  to  $360^\circ$ , achieved by rotating the half-wave plate in  $7.5^\circ$  increments from  $0^\circ$  to  $180^\circ$ . All spectra were acquired at ambient temperature with an exposure time of 5 s.

#### **Acknowledgements:**

P.L. acknowledges the support from the Postdoctoral Fellowship Program of China Postdoctoral Science Foundation (Grant No. GZC20241349). F.L. acknowledges the support from the National Key R&D Program of China (Grant No. 2023YFA1407100), and the National Natural Science Foundation of China (NSFC) (Grant Nos. 12474392 and 12074303).

#### **Author contributions:**

P.L. conceived the project and experiments. Y.G. conducted the experiments. P.L., Y.Y., and F.L. performed the theoretical calculations and electromagnetic simulations with Mathematica<sup>®</sup>. P.L. and Y.G. analyzed the data. P.L. and F.L. supervised the project and wrote the manuscript with input from all the other authors.

#### **Competing interests:**

The authors declare no competing interests.

#### **Data and materials availability:**

All data needed to evaluate the conclusions in this manuscript are available in the main text or the supplementary materials.



**Figures:**

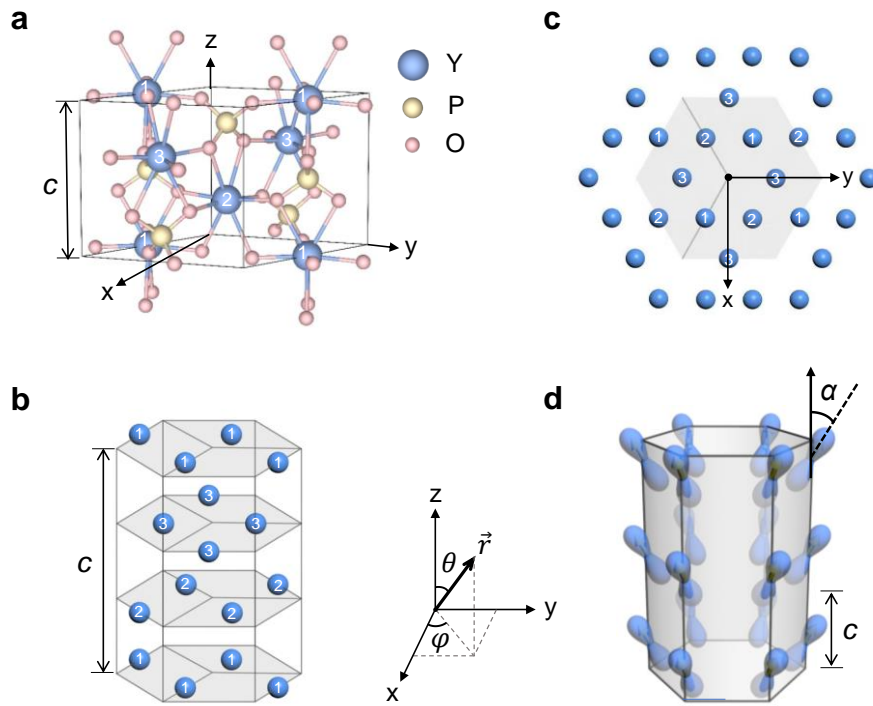


**Fig. 1 | Symmetry analysis of  $\text{Eu}^{3+}$  dopants and their optical magnetic transition dipoles within single hexagonal  $\text{YPO}_4$  crystal.** **a** Unit cell structure of the hexagonal  $\text{YPO}_4$  crystal. The x-y-z Cartesian coordinate system is defined with the z-axis parallel to the crystallographic c-axis (the long axis of the single crystal). **b** Distribution of  $\text{Y}^{3+}$  ions within the unit cell. Three layers of  $\text{Y}^{3+}$  ions are arranged along the c-axis in an ABCA stacking sequence. **c** Projection of the  $\text{Y}^{3+}$  lattice onto the x-y plane. They form a Kagome lattice with sixfold rotational symmetry. When they are fully or partially substituted by the  $\text{Eu}^{3+}$  dopants, the projection of the  $\text{Eu}^{3+}$  ions also exhibit sixfold rotational symmetry. **d** Equivalent physical model of optical magnetic transition dipoles of the  $\text{Eu}^{3+}$  ions within the single crystal. The polar angle  $\alpha$  represents the angle between the dipole and the crystal c-axis. In the inset,  $\vec{r}$  denotes the vector of far-field point, and  $(\theta, \varphi)$  represents the directional information of the far-field point.

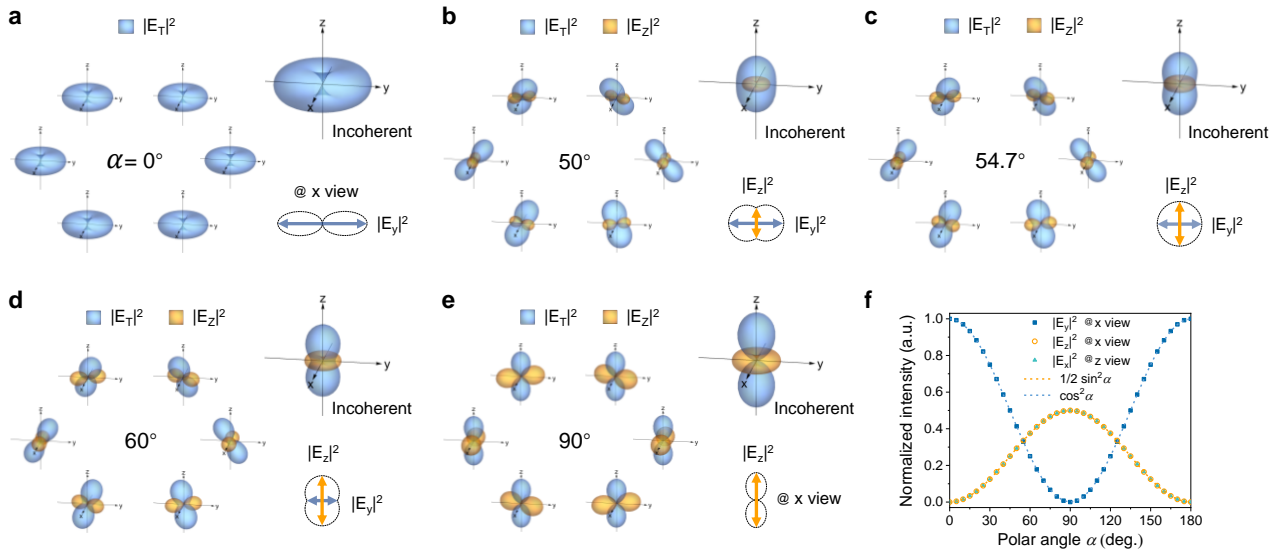


**Fig. 2 | Evolution of far-field polarized intensities as a function of the polar angle  $\alpha$ .** **a**  $\alpha = 0^\circ$ . **b**  $\alpha = 50^\circ$ . **c**  $\alpha = 54.7^\circ$ . **d**  $\alpha = 60^\circ$ . **e**  $\alpha = 90^\circ$ . The left side, top-right corner, and bottom-right corner show the far-field polarized intensities from the transition dipoles with sixfold rotational symmetry, their incoherent emission, and the schematic of linearly polarized intensities detected from the x-direction of the incoherent emission (the radial direction of the single microcrystal), respectively.  $|E_z|^2$  (yellow) and  $|E_T|^2$  (blue,  $|E_T|^2 = |E_x|^2 + |E_y|^2$ ) represent the linearly polarized intensities with electric vectors parallel and perpendicular to the crystal c-axis, respectively. **f** Normalized curves of the far-field polarized intensities at different detecting directions for a single-particle crystal as a function of the polar angle  $\alpha$ .

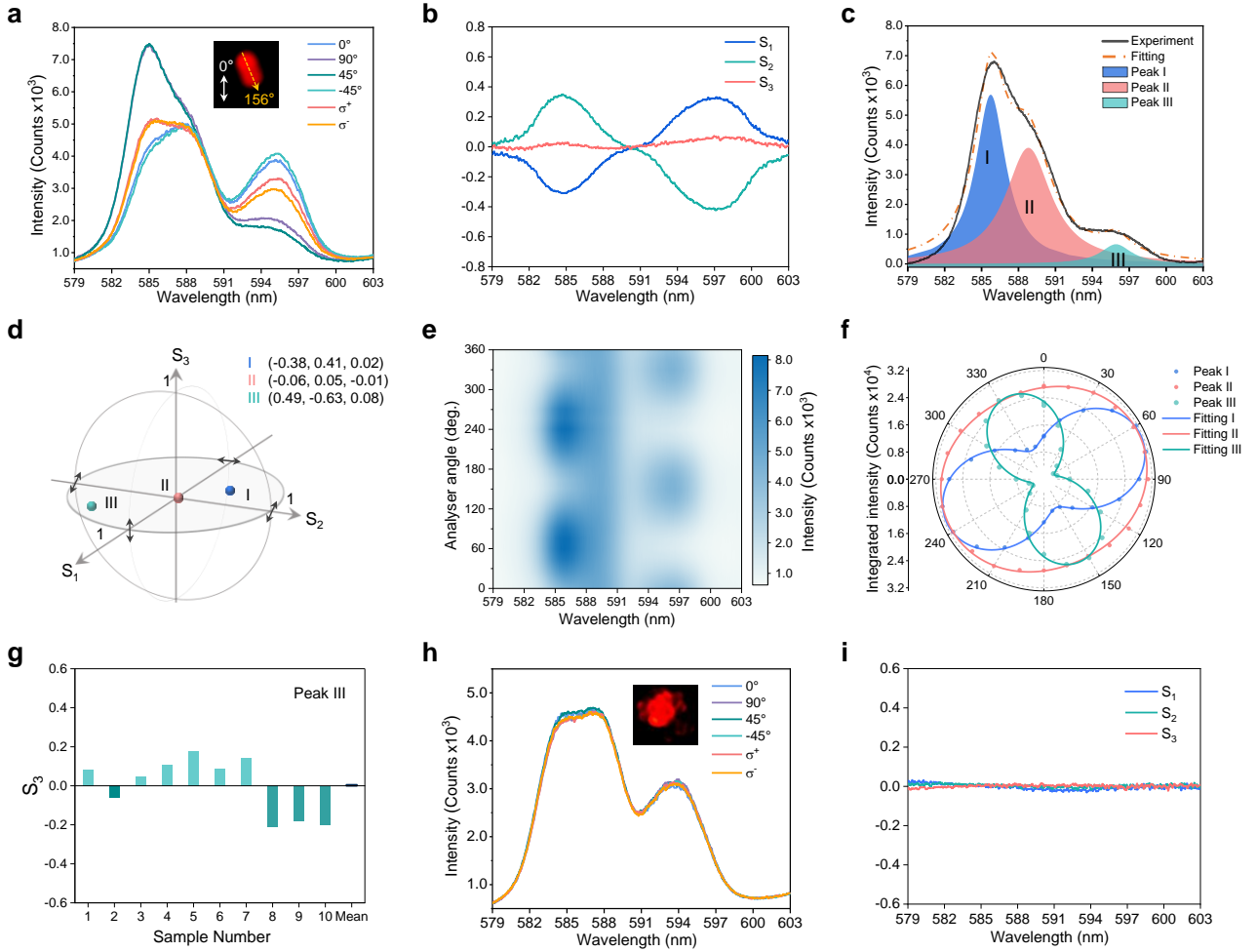


**Fig. 3 | Analysis of polarized photoluminescence (PL) of a single  $\text{YPO}_4:\text{Eu}^{3+}$  microcrystal (labeled as sample no. 1) and the ensemble. **a** Polarization analysis using Poincaré sphere (PS) method. Polarized PL spectra of the  $^5\text{D}_0 \rightarrow ^7\text{F}_1$  magnetic transition of  $\text{Eu}^{3+}$  dopants in a single microcrystal are recorded at the six Stokes bases, respectively. The inset is a CCD image showing the luminescent microcrystal lying on a substrate plane whose axis of length (crystalline c-axis) is oriented with an angle of  $156^\circ$  to the spectrometer entrance slit which is defined as  $0^\circ$ . **b** Stokes parameters  $S_1$ ,  $S_2$ , and  $S_3$  calculated from the six polarized spectra. **c** Lorentzian fitting of the  $45^\circ$  polarized spectrum. The result indicates that the magnetic transition consists of three emission peaks. **d** Coordinates ( $S_1$ ,  $S_2$ ,  $S_3$ ) for the three peaks in the polarization Poincaré sphere. **e** Intensity variation of the transition under continuous detection by linear polarization. **f** Polarization fitting (PF) analysis of the three emission peaks. **g** Statistical  $S_3$  values for the peak III from the ten random single microcrystals. **h** Polarization analysis of an ensemble of single microcrystals using the PS method. The inset is a CCD image of the luminescent ensemble. **i** The  $S_1$ ,  $S_2$ , and  $S_3$  of the ensemble. The results of  $S_1 = S_2 = S_3 = 0$  demonstrates the racemic nature and unpolarized luminescence of the ensemble.**

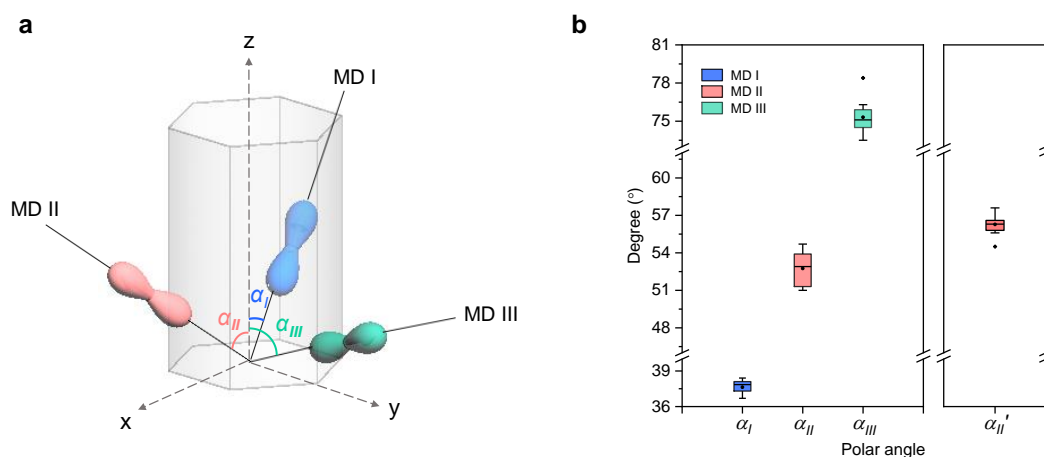


**Fig. 4 | Analysis of the magnetic transition dipole orientations in the single microcrystals. a** Schematic illustration of three magnetic dipole orientations corresponding to the three emission peaks, respectively.  $\alpha_I$ ,  $\alpha_{II}$ , and  $\alpha_{III}$  represent the polar angles between the three dipoles and the crystal c-axis (z-axis), respectively. **b** Statistical analysis of  $\alpha_I$ ,  $\alpha_{II}$ , and  $\alpha_{III}$  values calculated from the LDOPs of the three peaks for the ten single microcrystals based on the PF method.  $\alpha'_{II}$  (shown on the right) represents the theoretical orientation of the transition dipole II, as derived from the  $\alpha_I$  and  $\alpha_{III}$  values using the selection rules of  $D_2$  point group.

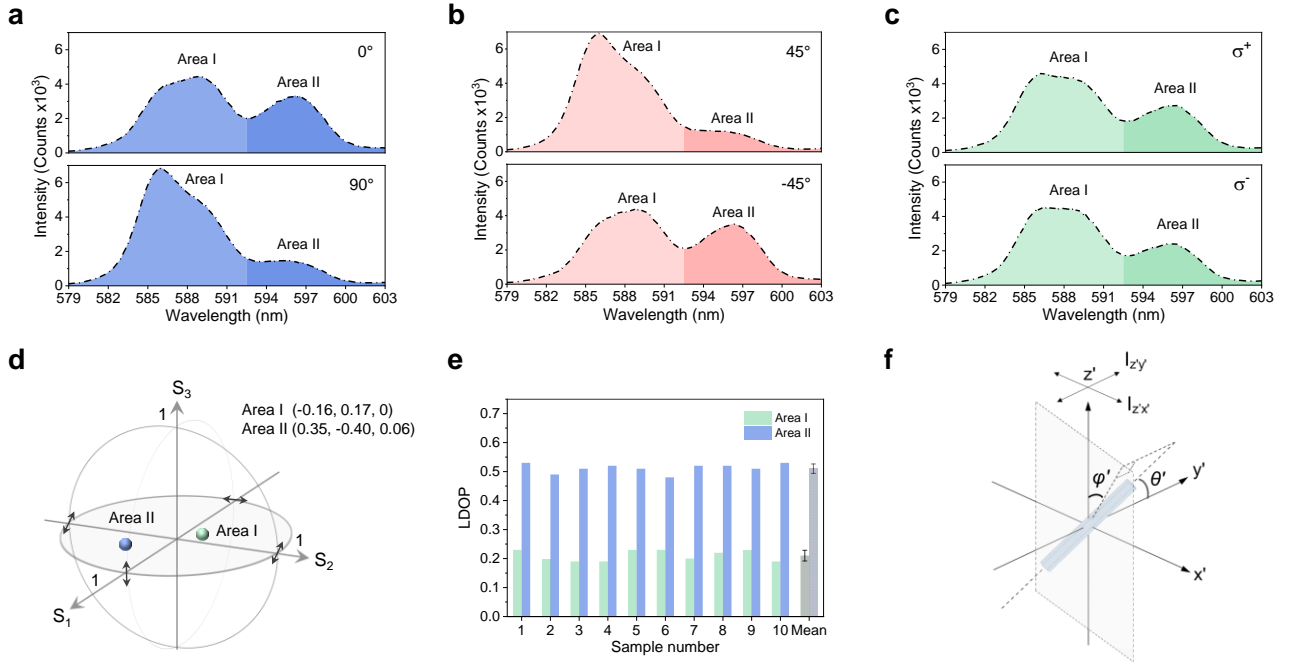


**Fig. 5 | Three-dimensional (3D) orientation determination of a single particle via spectral transition bands.** **a-c** Polarized analysis of the magnetic transition bands of the single  $\text{YPO}_4:\text{Eu}^{3+}$  microcrystal (sample no. 1) using the PS method. The selected bands I and II are in wavelength ranges of 579-592.5 nm and 592.5-603 nm, respectively. **d** Coordinates of the two transition bands in the polarization Poincaré sphere. Their locations on the equator plane indicates partially linear polarization. **e** Statistical analysis of the LDOPs of the two bands for the ten single microcrystals. The average values and standard deviations are presented in the right column. The small standard deviations highlight the robustness of the LDOPs for the transition bands. **f** Schematic illustration of 3D orientation determination of a single micro- or nanocrystal. In the defined Cartesian coordinate system,  $\theta'$  and  $\phi'$  represent the polar and azimuthal angles of the orientation of the crystal c-axis, respectively.  $I_{z'x'}$  and  $I_{z'y'}$  represent the orthogonally polarized intensities emitted along the  $z'$ -direction, respectively.